Supplementary Information Appendix

for

Universal Inverse Design of Surfaces with Thin Nematic Elastomer Sheets

Hillel Aharoni, Yu Xia, Xinyue Zhang, Randall D. Kamien, and Shu Yang

This document includes:

Materials and Methods

Numerical Inverse Design of 2D Metric Tensor

The inverse design problem for thin planar nematic elastomer sheets was presented by Aharoni *et al.* [S1]. It involves, given a desired two-dimensional metric tensor $\overline{a}$, finding coordinates $\{u, v\}$ in which $\overline{a}$ takes the form

$$\overline{a}(u,v) = R[\theta(u,v)] \begin{pmatrix} \lambda^2 & 0 \\ 0 & \lambda^{-2\nu} \end{pmatrix} R[\theta(u,v)]^T \qquad (S1)$$

for some director field $\theta(u,v)$. Here, λ and $\lambda^{-\nu}$ are the local expansion ratios parallel and perpendicular to the nematic director field and R is a planar rotation matrix. Aharoni *et al.* further pose this problem as finding a coordinate transformation with constraints on the transformed metric tensor's eigenvalues (or equivalently, on the singular values of the transformation Jacobian). It is not known whether such coordinates always exist, and therefore, in the general case, this search becomes an optimization problem; finding coordinates whose Jacobian's singular values best match the desired ones at every point, *i.e.* minimize a "parameterization energy" functional:

$$E[\boldsymbol{u}] = \iint dist^2(J(\boldsymbol{u}), \mathcal{D})\, dS\,, \qquad (S2)$$

where $\boldsymbol{u}$ is the parameterization, $J(\boldsymbol{u})$ the Jacobian of the transformation from $\boldsymbol{u}$ to local Riemann normal coordinates, and $\mathcal{D} \subseteq GL(2,\mathbb{R})$ is the set of desired local Jacobians, namely, in our case, $\mathcal{D} = \left\{ U \begin{pmatrix} \lambda & 0 \\ 0 & \lambda^{-\nu} \end{pmatrix} V^T \mid U, V \in SO(2) \right\}$. The function $dist$ may be any reasonable distance function, e.g. some matrix norm.

From this point of view, the inverse design problem is similar to other problems of finding optimal parameterizations of a surface, *e.g.* optimizing area preservation or angle preservation, many of which are highly applicative in computer graphics. For that goal, a discretized version of eq. $(S2)$ is often used:

$$E[\boldsymbol{u}, \{L_t \in \mathcal{D}\}] = \sum_{t \in \triangle} A_t \| J_t(\boldsymbol{u}) - L_t \|^2\,, \qquad (S3)$$

where t is taken over all mesh triangles, A_t and J_t are the areas and Jacobians respectively, and L_t are the locally best-matching "allowed" Jacobians (optimization is performed over both $\boldsymbol{u}$ and $\{L_t\}$). Here $\|\cdot\|$ is taken to be the Frobenius norm, $\|A\|^2 = \mathrm{Tr}[A^T A]$.

An efficient numerical scheme for optimizing eq. $(S3)$ was presented in the seminal work of Liu *et al.* [S2]. Their approach, coined *Local/Global*, breaks the nonlinear optimization process into a sequence of iterations, each composed of two linear steps; a local step, in which the local Jacobian $J_t(\boldsymbol{u}^0)$ at every mesh triangle separately is approximated by the best-matching $L_t \in \mathcal{D}$; a global step, in which $\{L_t\}$ are assumed fixed, and a global parameterization $\boldsymbol{u}$ which minimizes E

is chosen (by fixing the L_t's this becomes a linear problem). If $E[\boldsymbol{u}, \{L_t\}] < E[\boldsymbol{u}^0, \{L_t^0\}]$, this process can be repeated until converging. If the convergence energy is zero (or a numerical approximation of it), than we have found a parameterization that everywhere follows the local singular value rule (or a numerical approximation of it). As a useful side effect, the singular value decomposition of the obtained L_t's gives us the director field at every mesh triangle.

We employ the algorithm presented in [S2] using Matlab. We execute the local step by running singular value decomposition on the local 2×2 Jacobian at every mesh triangle, hence we get $J_t = USV^T$ where $U, V \in SO(2)$ and S a diagonal matrix with eigenvalues ordered from large to small. We then define $L_t = U \begin{pmatrix} \lambda & 0 \\ 0 & \lambda^{-\nu} \end{pmatrix} V^T$. It is important to note that the solution at any triangle is completely independent of solution in neighboring triangles. Therefore, if we were to run the local/global algorithm on an arbitrary initial parameterization, we would typically get a very "noisy" limit parameterization, stuck at some local equilibrium, with director field (principal direction) changing on the scale of a single triangle. To avoid that, we run the entire local/global algorithm twice. The first run is made with $\lambda = 1$. This poses a very tight restriction on $\mathcal{D}$ as a result of the eigenvalue degeneracy, and the process typically converges to a parameterization with high residual energy $(S3)$, commonly referred to as an "as rigid as possible" (ARAP) parameterization. We then stretch the entire coordinate space $\boldsymbol{u} \to \begin{pmatrix} \lambda & 0 \\ 0 & \lambda^{-\nu} \end{pmatrix} \boldsymbol{u}$ to align the local Jacobians, and run the local/global algorithm again with the desired λ and ν. Using the stretched ARAP parameterization as an initial condition typically results in a smooth, low-residually-stretched solution.

Numerical Inverse Design of 2D Curvature Tensor

It was shown in [S1] that a planar director field that is not homogeneous across the sheet's thickness, but rather changes from $\theta(u,v) + \Delta\theta(u,v)/2$ at one side to $\theta(u,v) - \Delta\theta(u,v)/2$ at the other side, where $|\Delta\theta| \ll 1$, induces on a nematic elastomer sheet the reference metric given by eq. $(S1)$ (with $O(\Delta\theta)^2$ corrections) along with a reference curvature tensor

$$\overline{b} = \frac{\lambda^2 - \lambda^{-2\nu}}{2h} R[\theta] \begin{pmatrix} 0 & 1 \\ 1 & 0 \end{pmatrix} R[\theta]^T \Delta\theta + O(\Delta\theta)^3. \qquad (S4)$$

In the thin limit, the ground state of a free elastic shell tends toward an isometry of its reference 2D metric tensor, which, among all isometries, minimizes the discrepancy between its curvature tensor and the shell's reference curvature tensor [S3]. For this reason, we first use the protocol described in the previous section to find a director field $\theta(u,v)$ that gives approximately the metric of our desired surface, and then use it as a given parameter in eq. $(S4)$ to induce $\overline{b}$ that is as close as possible to our desired surface's curvature tensor $\tilde{b}$. Although we in fact search for $\Delta\theta(u,v)$ that minimizes the bending energy functional, we use the less accurate yet simpler process of finding a minimizer to the Frobenius norm $\iint \mathrm{Tr}\left[\left(\overline{b} - \tilde{b}\right)^2\right] du\, dv$. Together with $(S4)$, the minimizer is given by

$$\Delta\theta = \frac{2h}{\lambda^2 - \lambda^{-2\nu}} \mathrm{Tr}\left(R[\theta] \begin{pmatrix} 0 & 1 \\ 1 & 0 \end{pmatrix} R[\theta]^T \tilde{b}\right) = \frac{4h}{\lambda^2 - \lambda^{-2\nu}} \left(R[\theta]^T \tilde{b}\, R[\theta]\right)_{uv} \qquad (S5)$$

where $(\cdot)_{uv}$ denotes the off-diagonal matrix element in the $\{u, v\}$ coordinates and h is the thickness of the sheet.

We evaluate the curvature tensor $\tilde{b}$ of our desired triangulated surface at the centers of mesh triangles using standard methods [S4]. Combined with the director field θ at mesh triangles we get from the protocol at described in the previous section and the explicit recipe $(S5)$, we obtain two planar director fields evaluated at mesh triangles, $\theta \pm \Delta\theta/2$, which we wish to impose upon the top and bottom surfaces of our thin nematic elastomer sheet. We thus create two masks – one for treating the top surface and one for treating the bottom surface (as described in Supplementary Text).

Materials

1,3-propanedithiol, 1,8-Diazabicyclo(5.4.0)undec-7-ene (DBU), butylated hydroxytoluene (BHT) and photoinitiator 2,2-dimethoxy-2-phenylacetophenone (DMPA) were purchased from Sigma Aldrich and used as received. Hydrochloric acid (HCl) was purchased from Fisher Scientific, and (tridecafluoro-1,1,2,2-tetrahydrooctyl)trichlorosilane (Silane-8174) was purchased from Gelest. Positive-tone photoresist, S1813 and epoxy resin D.E.R. 354 were purchased from Dow Chemical Company. Poly(dimethylsiloxane) (PDMS) precursor and curing agent, Sylgard ® 184, were purchased from Dow Corning. LC monomer, 1,4-bis- [4-(6-acryloyloxy-hexyloxy)benzoyloxy]-2-methylbenzene (RM82), was purchased from Wilshire Technologies Inc. and used without further purification.

Synthesis of LC Precursors

LC precursors were synthesized following the procedure reported earlier [S5]. $10g$ of RM82 and $3.14g$ of 1,3-Propanedithiol (PDT) (mol ratio of RM82 : PDT=1:2) were dissolved into $100mL$ CH_2Cl_2 with rigorous stirring. 2 drops of 1,8 Diazabicycloundec-7-ene (DBU) were then added as catalyst. The reaction mixture was stirred at room temperature overnight.

After reaction, the mixture was washed with diluted HCl twice (1M first and 0.1M 2nd), followed by washing with DI water once. The CH_2Cl_2 solution was then dried with $MgSO_4$ for 30min, and filtered afterwards. The final product (RM82-PDT) was collected as viscous liquid after evaporating the solvent under vacuum.

Fabrication of Epoxy 1D Channels

Masters with 1D channels were fabricated from photoresist S1813 using direct laser writing (Heidelberg DWL 66+). Glass substrates were pre-cleaned by rinsing with acetone three times, followed by drying with an air gun. A thin layer of S1813 (thickness $\sim 2\mu m$) was spin-coated (4000rpm for 40s) on the clean glass substrate, followed by prebaking at $110°C$ for 1 min. The S1813 photoresist layer was then exposed by direct writing laser (365nm UV light) with a designed pattern. After laser writing, the sample was developed by photoresist developer (MF319) to obtain the final S1813 pattern.

A PDMS mold was replicated from the S1813 master following the procedure reported in [S6].

To create 1D channels with planar anchoring to align LCMs, the PDMS mold was replicated to epoxy (D.E.R. 354). One drop ($\sim 10\mu L$) of D.E.R. 354 liquid was first placed on a clean glass, followed by covering the uncured epoxy liquid with the patterned PDMS mold. The epoxy liquid was then filled into the PDMS pattern through capillary infiltration. The D.E.R. 354 along with the PDMS mold was exposed to 365nm UV light with a dosage of 15,000 mJ/cm^2 to fully cure the epoxy. The final replica of epoxy was obtained by carefully peeling off the PDMS mold from the cured epoxy pattern.

Surface Coating of Epoxy Patterns

The as-prepared epoxy patterns were cleaned with a UVO cleaner (Jelight Company, Model 144AX) for 15min to slightly oxidized the epoxy surface. The samples were then moved to a vacuum chamber for fluoro-silane treatment through a chemical vapor deposition (CVD) process. A small drop ($\sim 5\mu L$) of fluoro-silane (Silane-8174) was placed at the center of the vacuum chamber surrounding by epoxy samples with similar distance towards the center droplet. As the chemical vapor pressure of the silane is dependent on its diffusion length, this would ensure a relatively uniform coating density on the epoxy samples. The chamber was then vacuum pumped for 25 min, and the final fluoro-silane coated (F-coated) samples were kept in a dry place for future use. The primary objectives of fluoro-silane coating are two folds: 1) F-coated epoxy gives planar anchoring towards the mixture of RM82 and RM82-PDT. 2) F-coating is well-known as low surface energy material for easy boundary delamination to separate LCE films from the epoxy patterns.

Preparation of LCE Sheets

The F-coated epoxy substrates were used as both the top and the bottom surfaces to construct the LC cells; they were aligned under an optical microscope with a mismatch $< 10\mu m$. The top and bottom channels were individually designed to construct a small twisting angle across film thickness following theoretical calculation. The thickness of the LC cells was controlled using Mylar (either 150 or $100\mu m$ thick) as spacer. After aligning the two epoxy patterns, the two substrates were then fixed by epoxy glue on the two edges of the sample.

To prepare LCM precursors, RM82 and RM82-PDT were mixed with a molar ratio 1:1 in a 5 mL vial, and ~1 wt% of DMPA was added as photoinitiator. Due to the high active nature of thiol-acrylate reaction, 0.1 wt% free radical inhibitor (BHT) was added to avoid polymerization before UV exposure. The mixture was melted on a hot stage at $100°C$ with vigorous stirring until fully mixed. To prevent reaction between RM82 and RM82-PDT while heating, short mixing time is preferred (1-2 min).

After full mixing, the mixture of LCM precursor was then infiltrated into the epoxy LC cell on the hot stage at $100°C$ through capillary force. The LC cell was then moved to a $60°C$ hot stage and annealed for 45 min to achieve LC alignment. The alignment of LCM in the cell was confirmed by polarized optical microscope (POM). LC cell was then exposed to UV irradiation (365nm, Newport model 97436-1000-1, Hg source) at a dosage of 1000-10K mJ/cm^2, and the final LCE sheets were obtained by peeling the thin film off the epoxy patterns.

Characterization

Differential Scanning Calorimetry (DSC): DSC tests were performed on a TA Instruments Q2000 with an aluminum hermetic crucible. Sample was heated and cooled with ramping rate $10°C/min$ for three cycles, and data from the 2nd cycle was reported. Oligomer mixture of RM82/RM82-PDT was scanned from $120°C$ to $-40°C$, and the crosslinked LCE film was scanned from $180°C$ to $-30°C$. For the DSC measurement of the oligomer mixture, 0.1 wt% of BHT was added to avoid thermal polymerization during heating and cooling cycles, and the final data showed the three cycled curves are mostly identical. For the measurement of crosslinked LCE film, a polydomain sample was used and cut into small pieces to be contained in the aluminum crucible without mechanical pressing, and the DSC data showed a weak nematic to isotropic phase transition near $130°C$. This phase transition was also seen under POM during the measurement of actuation strain under heating. It should be noted that after the phase transition, the nematic phase still holds a significant amount of order parameter that gradually decreases with the increasing temperature till $180°C$. DSC also found a glass transition temperature of the LCE film around $0°C$, indicative of elastomeric nature of the crosslinked membrane.

Gel Permeation Chromatography (GPC): GPC was performed on a Tosoh EcoSEC GPC system with tetrahydrofuran as eluent at a flow rate of 1 mL/min. To ensure the separation of the oligomers, RM82-PDT sample was permeated through a combination of three single-pore gel columns (Tosoh). And the molecular weight of polymers in RM82-PDT was calculated by using polystyrene standards (Sigma Aldrich), as shown in Fig. S2.

Tensile Testing: Tensile testing was performed on an Instron machine (Instron Model 5564, with a 10 N load cell) under displacement control (10 mm/min). Rectangular samples (20 mm × 10 mm × 0.15 mm) were cut from a uniformly aligned samples and tested with the LC director either parallel or perpendicular to the displacement direction. As shown in Fig. S4b, the modulus of LCE is much higher in the director direction comparing to that in the perpendicular direction.

Polarized Optical Microscopy (POM): LC alignment was characterized by a motorized optical microscope (Olympus BX61) equipped with crossed polarizers using CellSens software. Heating and cooling of samples were performed in ambient air on a Mettler FP82 and FP90 thermo-system hot stage. POM was also used to monitor dimensional change of monodomain LCE films for the measurement of actuation strain. The actuation strain was calculated from the dimensional change of a small rectangular piece of monodomain LCE film floating on a thin layer of silicon oil upon heating on the hot stage. Images were taken with $10°C$ temperature intervals at a heating rate of $1°C/min$. Dimension of the films were directly measured from the images using CellSens software.

LCE Actuation Characterization: For thermal actuation, samples were heated to $180°C$ at a heating rate $\sim 100°C/min$ in ambient air on a hot plate (IKA C-Mag HS7) and cooled to room temperature naturally. Films were typically heated and cooled for several cycles (3-4 times) to release residual stress before image and video capture. Instead of ambient light, directional light was used and carefully adjusted to minimize surface iridescent reflection that comes from the micro-channels on the sample surface. Images and videos of the actuating LCE sheets were taken by a digital camera.

Scanning Electron Microscopy (SEM) and Atomic Force Microscopy (AFM) Imaging: SEM imaging was performed on a dual beam FEI Strata DB 235 Focused Ion Beam (FIB) SEM instrument with 5KV electron beam. AFM imaging was performed on a Bruker Dimension Icon AFM under tapping mode.

Measurement of 3D topography: The 3D topography of the LCE face membrane (Fig. S7) was quantitatively measured by a Keyence VHX-5000 microscope. The 3D scan was taken while the LCE sample is heated to $180°C$ using a hot stage.

Supplementary text

LC anchoring control

LC anchoring on 1D channels is highly affected by the channel width and depth. The anchoring energy density follows Berreman's model [S7]:

$$\rho_{max} = \frac{\pi^2 K A^2}{\lambda^3} \qquad (S6)$$

where K is the average elastic constant of LCs, A and λ are the depth and pitch (width + spacing) of the channel, respectively. ρ_{max} is the anchoring strength of LCs on the 1D channels representing the potential of reorientation of LCs from other alignment directions to the channel direction. Our previous method [S8] created micro-channels through photolithography with $A = 1.5\mu m$ and $\lambda = 4\mu m$, and they worked nicely to create various topological defects. However, in our new LC oligomer system, it is found to be less effective: numerous unwanted defects are generated during the annealing process that strongly impedes uniform alignment. We suspect this to be attributed to the non-sufficient surface anchoring energy, and the sharp edges and corners of the channel pattern that could trap spurious topological defects. To circumvent this, we specially design our new channel patterns with smaller channel width and smoother surface topography, enabled by the advanced direct laser writing technique. Firstly, we spin-coated a $\sim 2\mu m$ thick positive-tone photoresist (S1813) onto a flat substrate. The film thickness was designed to be thicker than the desired channel depth such that only top of the photoresist will be developed to avoid the sharp bottom corners in the channel pattern. Secondly, we carefully adjusted the exposing laser power to secure the UV light only penetrated a small depth into the photoresist film. Because the uneven UV light distribution in the thickness of the photoresist layer that the top layer absorbs light more than the bottom layer, the obtained channel pattern would have a smooth surface topography, which was confirmed by SEM (Fig. S6a) and AFM (Fig. S6b) measurements. As shown from the SEM and AFM images, neither the top or the bottom of the channels has sharp edges and λ is reduced to $2\mu m$, which from eq. $(S6)$ would increase surface anchoring energy by 8 times. Therefore, with the reduced λ, LCs can achieve strong surface anchoring on much smaller surface corrugation/channel depth. Our finding shows that 600nm is the near-optimized channel depth in consideration of LC surface anchoring and lithographic fabrication.

Quantitative Measurement of the Gaussian Curvature

To further validate the inverse engineering approach, we performed quantitative measurement of a simple geometry, the constant positive Gaussian curvature sample in Fig. 4a and Movie S2. As we noted in experiments, and as can be seen in Movie S2, the LCE film is principally spherical, however it is slightly deformed around the corners, and appears to be less curved than expected at high temperatures. To quantify this, we measured the Gaussian curvature as a function of plate temperature, while heating at a rate of $\sim 100^{\circ}C/min$. Results are shown in Fig. S7. As seen there, the experimental and theoretical values agree well at temperatures at and below 140°C, but start to deviate at higher temperatures, as experimentally obtained curvatures are indeed overall lower. A major reason for that deviation is the temperature gradient; as temperature grows and the sample curves, its central region lifts further away from the hot plate, and is then at a lower temperature than that of the plate, resulting in curvature which is lower than that predicted for the plate temperature. In contrast, the corners remain close to the plate and are at their target temperature and curvature. Secondary reasons are gravity, which somewhat flattens the sample as its weight is carried by only the four corners, and friction, which hinders the corners sliding towards each other that is necessary for realizing the geometry of a high curvature sphere. Therefore, the non-ideal curvature at the higher temperature could be attributed to the combination of spatial temperature gradient, which is more severe at the higher temperature, gravity, and friction.

Inducing Reference Curvature

Even though inverse calculation from theory gives 2D director patterns, the parallel alignment of LC molecules across the LCE film results in multiple isometries of the shape transformation. As mentioned in the main text, we augment our design with imposing a slight twist of LC molecules from the top to the bottom of the film. The calculation of $\Delta\theta$, the angle difference between the top and bottom director fields for which the target shape minimizes bending energy among its isometries, is detailed in the Materials and Methods section. For the face sample in main-text Fig. 4, with film thickness $100\ \mu m$, we get an angle difference within the range $-3^{\circ} < \Delta\theta < 3^{\circ}$ over the entire sample.

In experiment, however, inducing reference curvature needs to serve several purposes (as discussed in the main text), one of which is to help the initially flat sheet buckle in the correct direction and dynamically move toward the preferred equilibrium shape. For that reason, we made several samples, in which we overexpressed the target curvature at every point ($\Delta\theta \rightarrow 2\Delta\theta$ over the entire sample) or just around the edges ($\Delta\theta \rightarrow \left(1 + 5e^{-d/2mm}\right)\Delta\theta$, with d the distance to the boundary), to check whether we can get better dynamical behavior and still have the equilibrium not far from our target shape. We noticed that the overly curved LCE films often deformed into relatively irregular shapes, far away from theoretical prediction. Films with the calculated $\Delta\theta$, for most of times, were able to find a route to the correct isometry, demonstrating the face shape. We show our best results in Fig. 4 and Supplementary Movie S4. We therefore conclude that using the direct calculation of $\Delta\theta$ described in Materials and Methods is preferable.

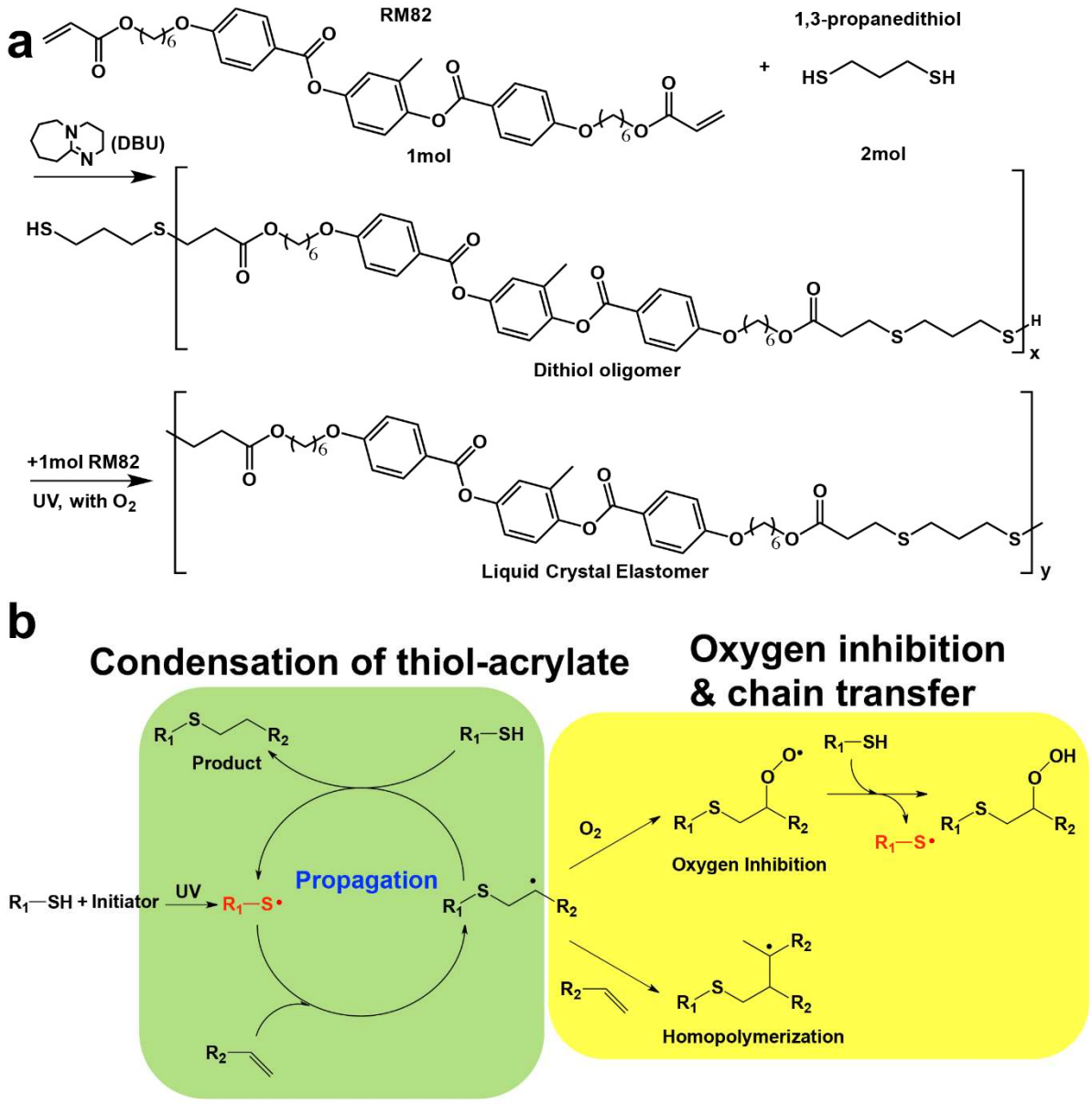

Fig. S1 Schematic illustration of (a) chemical reactions used in this work. (b) oxygen mediated thiol-acrylate "click" reaction. The oxygen here serves as a chain transfer agent that transfers the active free radical from the homopolymerization of acrylates to the condensation reaction of thiol-acrylate, which effectively lowers the crosslinking density of the system and results in an elastomeric polymer network.

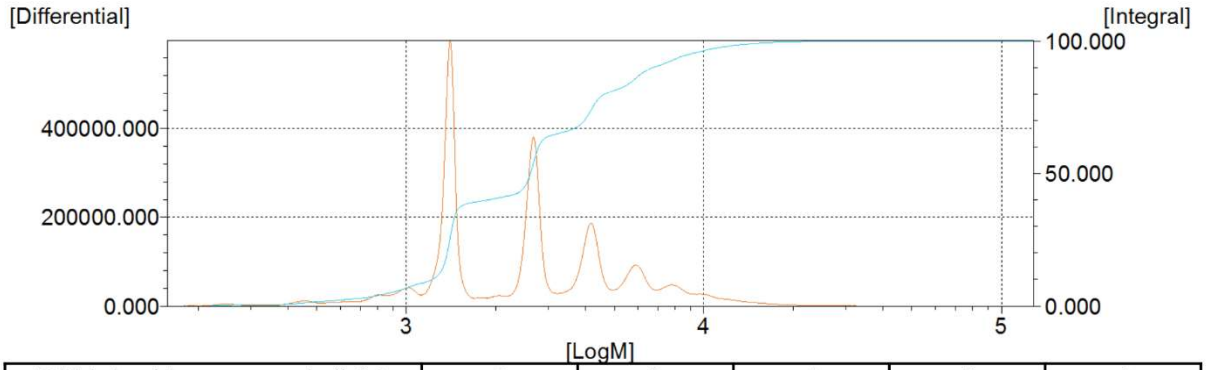

Dithiol with repeat unit # (x)	2	3	4	5	6
Mol fraction (%)	55.176	28.908	18.067	10.546	6.092

Fig. S2 Gel permeation chromatography (GPC) measurement of RM82-PDT. The fraction of each oligomer with different chain length is estimated from the area of the corresponding peak. One can clearly see the major part of the oligomer is short chain oligomers with repeat unit number x =2, 3, 4.

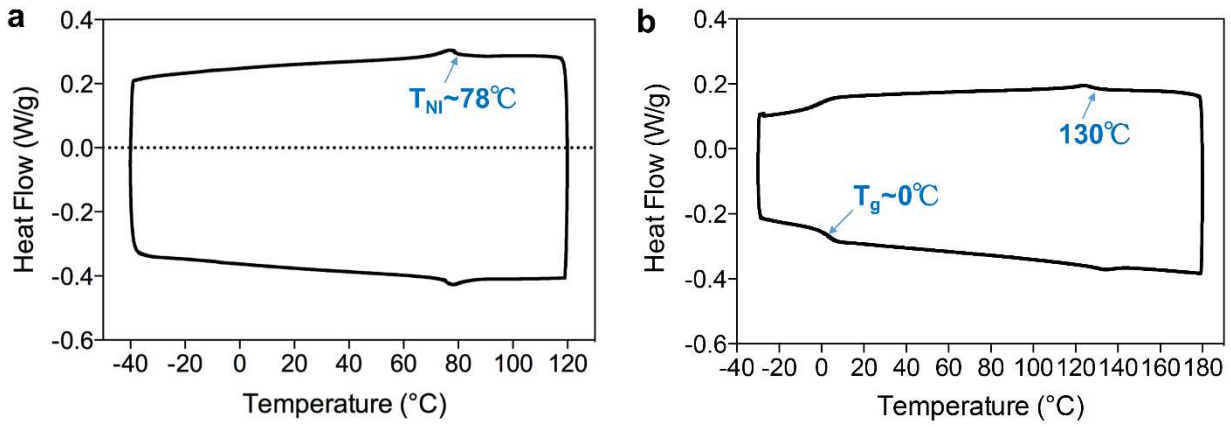

Fig. S3 Differential scanning calorimetry (DSC) measurements of LCM mixture (a) and the crosslinked LCE (b). (a) The nematic-isotropic phase transition temperature (T_{NI}) is found ~ 78ºC, and the LCM mixture shows no crystallization until -40 ºC. (b) The film shows an elastomeric characteristic with a T_g ~ 0 ºC, and an nematic-isotropic phase transition ~ 130 ºC.

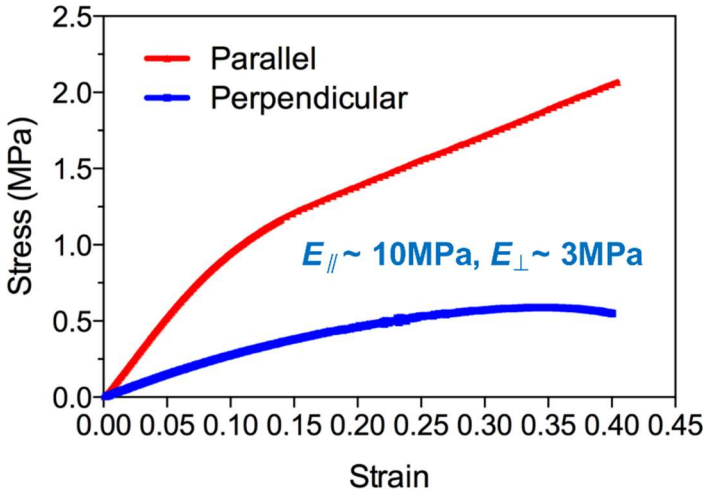

Fig. S4 Mechanical measurement of the stress-strain curves of the thiol-acrylate LCE film.

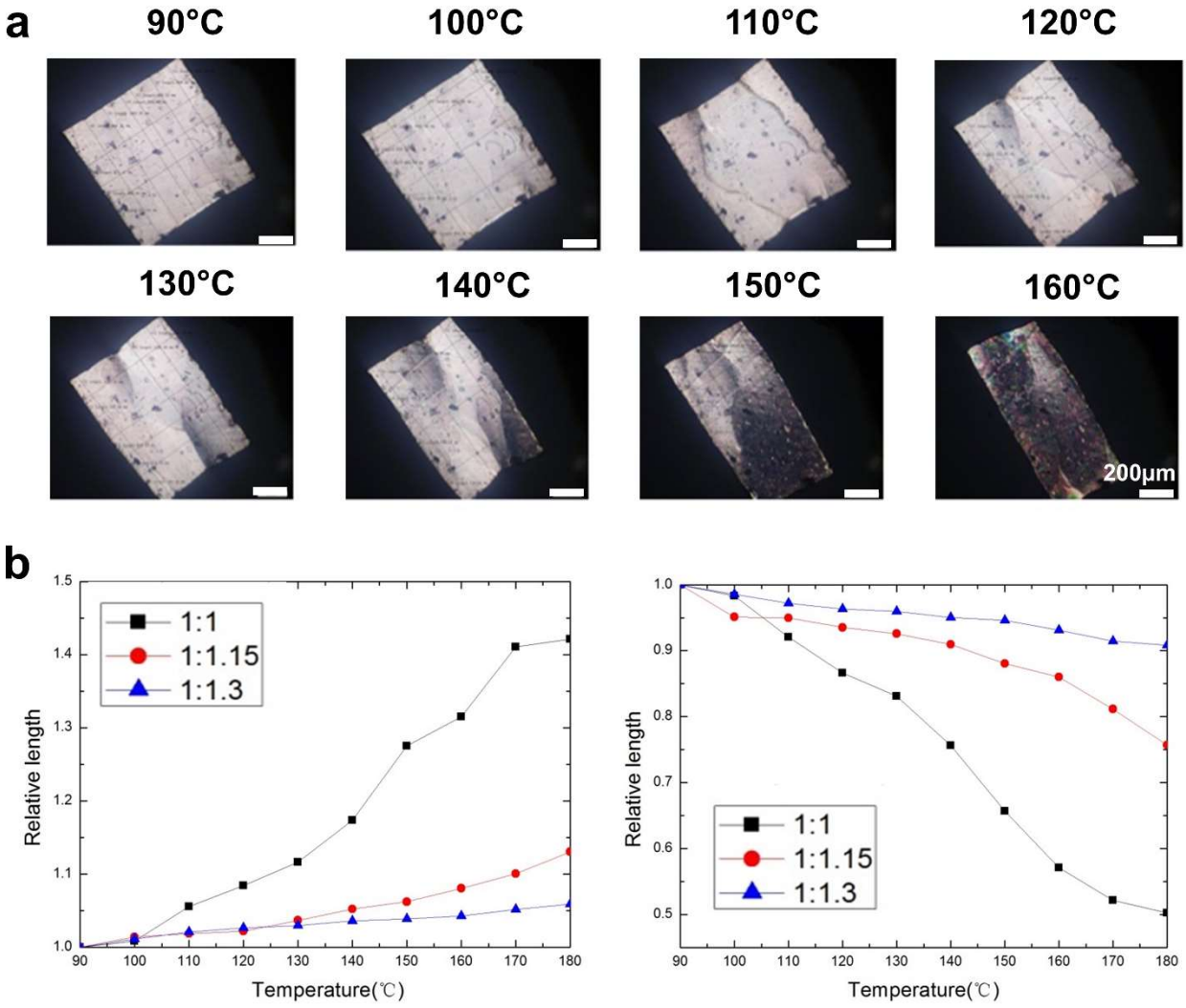

Fig. S5 Characterization of LCE film for thermal actuation. (a) POM images show the deformation of a uniformly aligned LCE film under heat. (b) Thermal actuation of LCEs with different crosslinking. Black, red and blue dots represent different molar ratio of RM82:dithiol from 1:1, 1:1.15 to 1:1.3, respectively.

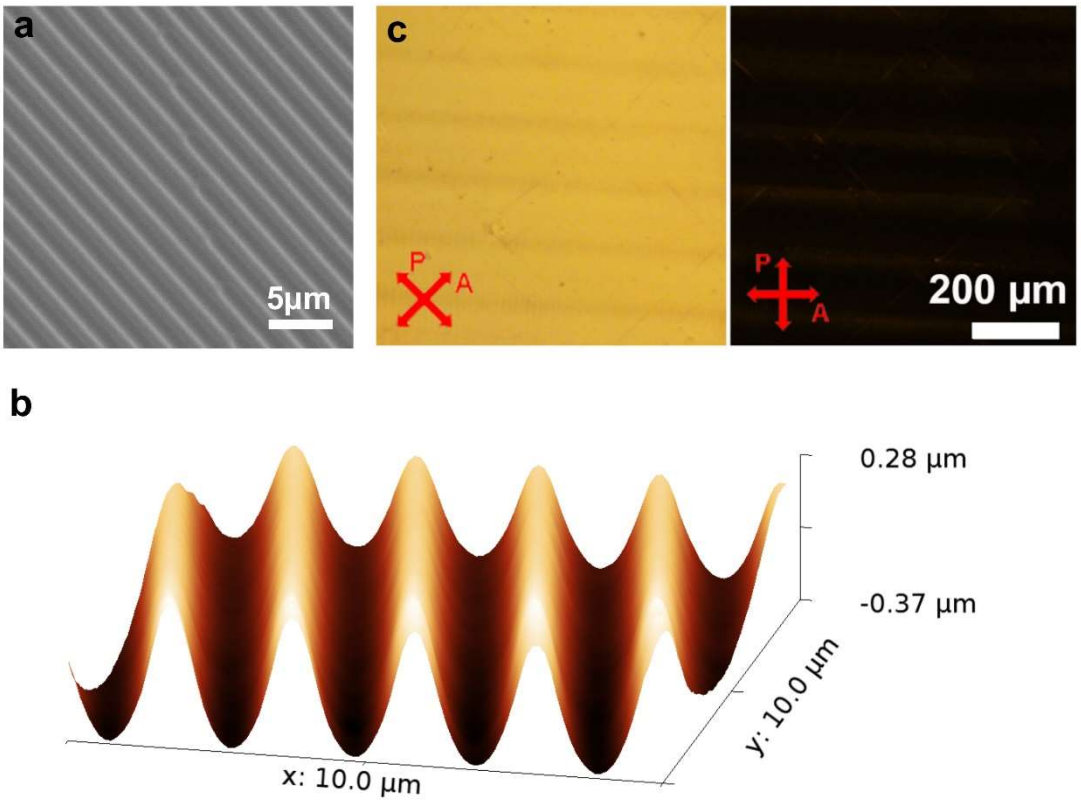

Fig. S6 Characterization of 1D channels and their LCM alignment property. (a) SEM image of 1D micro-channels. (b) AFM measurement of 1D micro-channles. (c) LCMs on top of 1D channels at 45º(left) and 0º(right) polarizer angle. Uniform LC alignment is strongly imposed by the 1D channels without any defect.

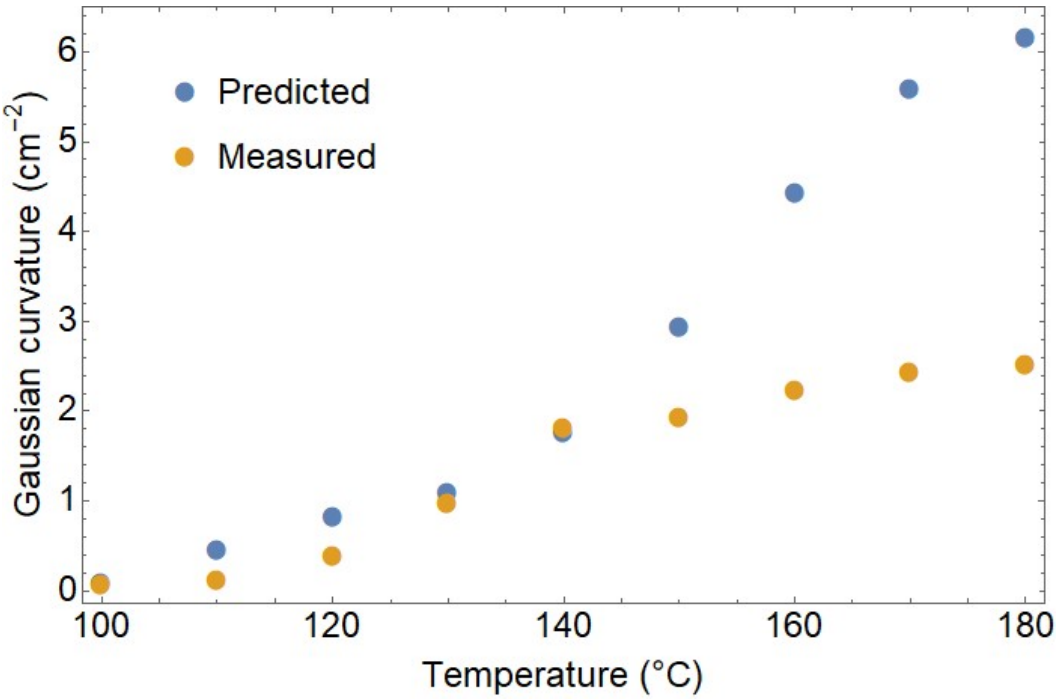

Fig. S7 Quantitative measurement of positive Gaussian curvature as a function of temperature. The experimentally measured values (yellow dots) are plotted in comparison with theoretical prediction (blue dots). The deviation between experiment and theory after 140°C is majorly subjected to a spatial temperature gradient, gravity and friction.

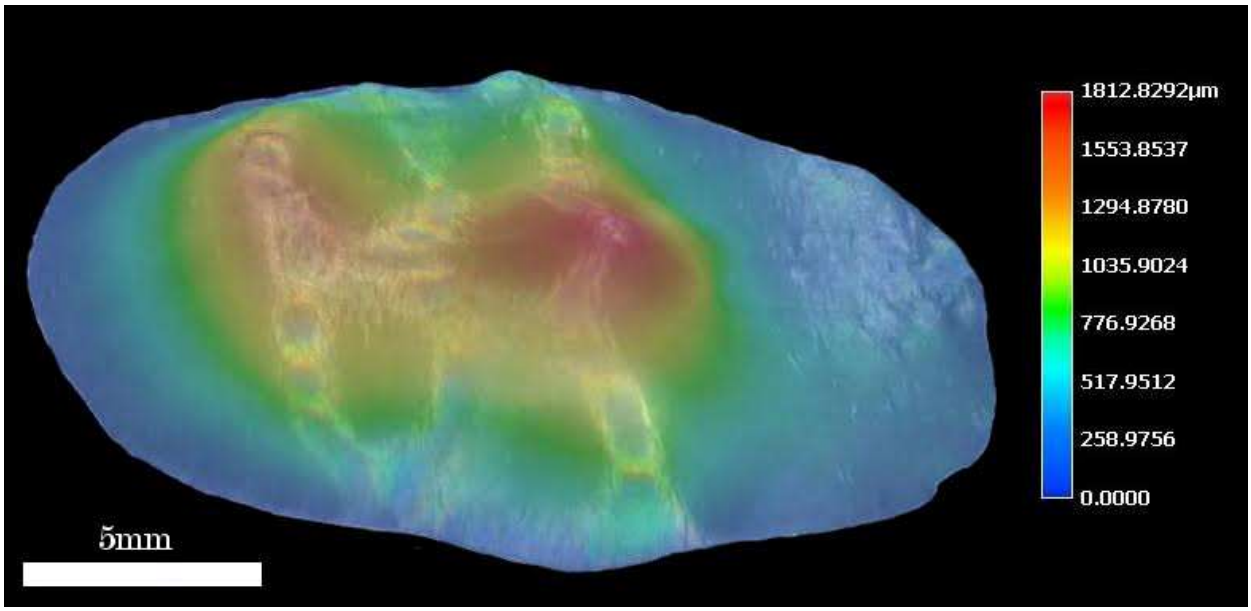

Fig. S8 Topography of the LCE face membrane at $180°C$. The 3D shape is presented using the local height of the buckled film. Colors corresponding to values of the height function are indicated by the color bar at the right.

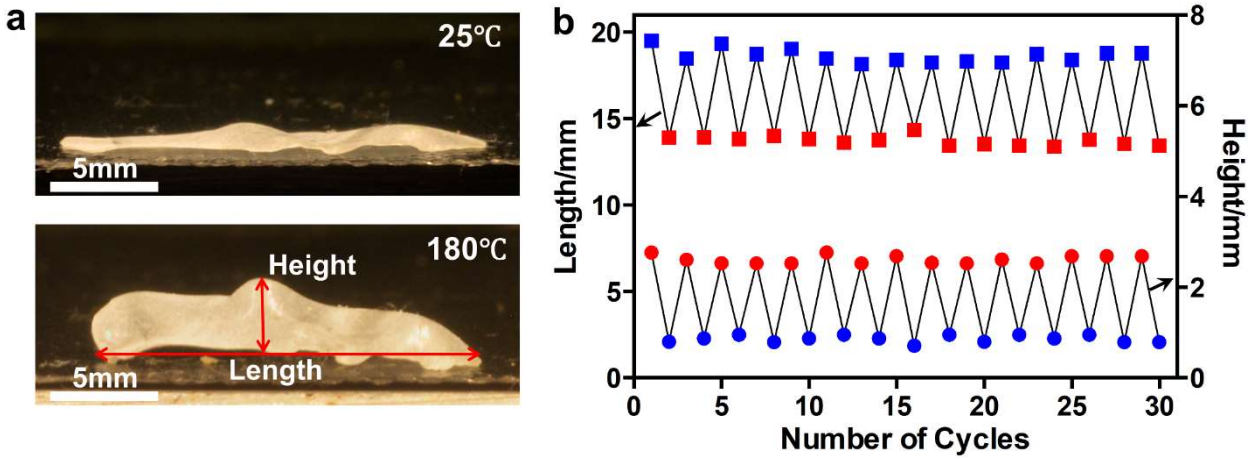

Fig. S9 Reversibility of LCE face. (a) Optical images showing side view of the LCE film at $25°C$ (top) and $180°C$ (bottom). (b) Measurements of the length (squares) and height (circles) of the LCE film during 30 consecutive heating and cooling cycles. Red and blue data points represent measurements at $180°C$ and $25°C$, respectively. No apparent change in the shape of the LCE face was found after 30 cycles.

Movie S1

LCE-type deformation visualized with Tissot's indicatrices. When the cylinder-shaped sheet is actuated, small circles transform into identical ellipses with principal axes $\{\lambda, \lambda^{-\nu}\}$, locally aligned with the director field explicitly calculated by Aharoni *et al.* in [S1]. The deformation globally transforms the cylinder into a sphere.

Movie S2

LCE sheet programmed to obtain constant positive Gaussian curvature, heated to $180°C$. Heating rate is $\sim 100°C/min$, video speed is $3.5 \times$ real time.

Movie S3

LCE sheet programmed to obtain constant negative Gaussian curvature, on a hot plate at $180°C$, shown while removed from the hot plate and then put back again. Video is in real time. The sample "dancing" is on account of the spatial temperature gradient (lower away from the hot plate).

Movie S4

LCE sheet programmed to obtain the shape of a leaf, heated to $180°C$. Heating rate is $\sim 100°C/min$, video speed is $3.5 \times$ real time.

Movie S5

LCE sheet programmed to obtain the shape of a face, heated to $180°C$. Heating rate is $\sim 100°C/min$, video speed is $3.5 \times$ real time. Some deviation from the target shape is visible in the lower and left sides of the face. These are largely on account of the sample boundaries being cut by hand by scissors, with no obvious visual guide.

References

[S1] Aharoni, H., Sharon, E. & Kupferman, R., Geometry of Thin Nematic Elastomer Sheets. *Phys. Rev. Lett.* **113** (25), 257801 (2014).

[S2] Liu, L., Zhang, L., Xu, Y., Gotsman, C. & Gortler, S. J., A local/global approach to mesh parameterization. *Eurographics Symp. Geom. Process.* **27** (5), 1495-1504 (2008).

[S3] Kupferman, R. & Solomon, J. P., A Riemannian approach to reduced plate, shell, and rod theories. *J. Funct. Anal.* **266** (5), 2989-3039 (2014).

[S4] Rusinkiewicz, S., *Estimating curvatures and their derivatives on triangle meshes*, presented at Proc. - 2nd Int. Symp. 3D Data Process. Vis. Transm. 3DPVT 2004, 2004.

[S5] Xia, Y., Zhang, X. & Yang, S., Instant Locking of Molecular Ordering in Liquid Crystal Elastomers by Oxygen-Mediated Thiol-Acrylate Click Reactions. *Angew. Chemie Int. Ed.*, doi.org/10.1002/anie.201800366 (2018).

[S6] Zhang, Y., Lo, C. W., Taylor, J. A. & Yang, S., Replica molding of high-aspect-ratio polymeric nanopillar arrays with high fidelity. *Langmuir* **22** (20), 8595-8601 (2006).

[S7] Berreman, D. W., Solid surface shape and the alignment of an adjacent nematic liquid crystal. *Phys. Rev. Lett.* **28** (26), 1683-1686 (1972).

[S8] Xia, Y., Cedillo-Servin, G., Kamien, R. D. & Yang, S., Guided Folding of Nematic Liquid Crystal Elastomer Sheets into 3D via Patterned 1D Microchannels. *Adv. Mater.* **28** (43), 9637-9643 (2016).

```
% Author: Hillel Aharoni

function [vt,ang,dang]=LCE(x,t,vt0,lambda,nu,FvK,tolerance)
% Input:
    % Desired surface (e.g. from .obj file);
        % x - 3D vertex coordinates
        % t - triangulation
        % vt0 - some 2D parameterization
    % Target parameters;
        % lambda - extension along director
        % nu - optothermal Poisson's ratio
        % FvK - Foppl-von Karman number of target sheet (for calculating dang)
    % tolerance - for energy convergence
% Output:
    % vt - output paramaterization
    % ang - director field for mid-surface
    % dang - director field difference between top and bottom

%% Precomputations %%
EV=EdgeVectors(x,t);
C=Cotangents(x,t);
L=Laplacian(x,t,C);
L1=L;
L1(1,size(L1,1)+1)=1;
L1(size(L1,1)+1,1)=1;
Linv = inv(L1);

%% First run of L/G algorithm for as-rigid-as-possible parameterization %%
E=-1;
Epre=0;
vt=vt0;
iterations=0;
while abs(Epre-E)>5*tolerance
    iterations=iterations+1;
    Epre=E;
    R=LocalStep(vt,t,EV,C,[1,1]);
    vt=GlobalStep(EV,Linv,t,C,R);
    E=Energy(EV,t,vt,C,R);
end

%% Stretch results by preferred deformation %%
deformation=[lambda, lambda^(-nu)];
vt=bsxfun(@times,deformation,vt);

%% Second run of L/G algorithm with preferred local deformation %%
while abs(Epre-E)>tolerance
    iterations=iterations+1;
    Epre=E;
    [R,ang]=LocalStep(vt,t,EV,C,deformation);
    vt=GlobalStep(EV,Linv,t,C,R);
    E=Energy(EV,t,vt,C,R);
end

%% Calculate angle difference to create reference curvauture %%
b=CurvatureTensor(x,t,vt);
dang=(cos(2*ang).*squeeze(b(1,2,:)+b(2,1,:))+sin(2*ang).*squeeze(b(2,2,:)-b(1,1,:)))/abs(diff(
deformation))/sqrt(FvK)/2;

end

function EV=EdgeVectors(x,t)
EV=zeros(size(t,1),3,2);
for i=1:size(t,1)
        v=x(t(i,:),:);
        dv=v([3,1,2],:)-v([2,3,1],:);
        [~,n]=lsqPlane(v);
        if n*cross(dv(1,:),dv(2,:))'<0, n=-n; end;
```

```
        dirs=cross(n,[1,0,0]); dirs=[dirs; cross(n,dirs)]'/norm(dirs);
        EV(i,:,:)=shiftdim(dv*dirs,-1);
end
end

function C=Cotangents(x,t)
C=[];
for i=1:size(t,1)
    idx1=t(i,1);
    idx2=t(i,2);
    idx3=t(i,3);
    v1=x(idx1,:);
    v2=x(idx2,:);
    v3=x(idx3,:);
    a=norm(v1-v2);
    b=norm(v2-v3);
    c=norm(v3-v1);
    angle1=acos((a^2+c^2-b^2)/(2*a*c));
    angle2=acos((a^2+b^2-c^2)/(2*a*b));
    angle3=acos((b^2+c^2-a^2)/(2*b*c));
    C(i,1)=cot(angle1);
    C(i,2)=cot(angle2);
    C(i,3)=cot(angle3);
end
end

function L=Laplacian(x, t, C)
n=size(x, 1);
L=sparse(n, n);
for i=1:size(t,1)
    for j=0:2
        j1=j+1;
        j2=mod(j+1,3)+1;
        j3=mod(j+2,3)+1;
        idx1=t(i,j1);
        idx2=t(i,j2);
        idx3=t(i,j3);
        L(idx1,idx1)=L(idx1,idx1)+C(i,j2)+C(i,j3);
        L(idx1,idx2)=L(idx1,idx2)-C(i,j3);
        L(idx1,idx3)=L(idx1,idx3)-C(i,j2);
    end
end
end

function [R ang]=LocalStep(u,t,EV,C,deformation)
R=zeros(size(t,1),4);
ang=zeros(size(t,1),1);
for i=1:size(t,1)
    idx1=t(i,1);
    idx2=t(i,2);
    idx3=t(i,3);
    u1=u(idx1,:);
    u2=u(idx2,:);
    u3=u(idx3,:);
    uu(1,:)=u3-u2;
    uu(2,:)=u1-u3;
    uu(3,:)=u2-u1;
    xx(1,1)=EV(i,1,1);
    xx(1,2)=EV(i,1,2);
    xx(2,1)=EV(i,2,1);
    xx(2,2)=EV(i,2,2);
    xx(3,1)=EV(i,3,1);
    xx(3,2)=EV(i,3,2);
    cc(1,1)=C(i,1);
    cc(2,2)=C(i,2);
    cc(3,3)=C(i,3);
    CovMat=xx'*cc*uu;
    [s,v,d]=svd(CovMat);
```

```
    l=diag(deformation);
    rot=d*s';
    ang(i)=asin(-d(1,2));
    if det(rot)<0
        if v(1,1)<v(2,2)
            s(:,1)=-1.0*s(:,1);
        else
            s(:,2)=-1.0*s(:,2);
        end
    end
    rot=d*l*s';
    R(i,1)=rot(1,1);
    R(i,2)=rot(1,2);
    R(i,3)=rot(2,1);
    R(i,4)=rot(2,2);
end
end

function U=GlobalStep(EV,Linv,t,C,R)
bx=zeros(size(Linv,1),1);
by=zeros(size(Linv,1),1);
for i=1:size(t,1)
    for j=0:2
        j1=j+1;
        j2=mod(j+1,3)+1;
        j3=mod(j+2,3)+1;
        idx2=t(i,j2);
        idx3=t(i,j3);
        Eij(1,1)=EV(i,j1,1);
        Eij(2,1)=EV(i,j1,2);
        rot(1,1)=R(i,1);
        rot(1,2)=R(i,2);
        rot(2,1)=R(i,3);
        rot(2,2)=R(i,4);
        bx(idx3) = bx(idx3)+rot(1,:)*Eij*C(i,j1);
        bx(idx2) = bx(idx2)-rot(1,:)*Eij*C(i,j1);
        by(idx3) = by(idx3)+rot(2,:)*Eij*C(i,j1);
        by(idx2) = by(idx2)-rot(2,:)*Eij*C(i,j1);
   end
end
bx(size(Linv,1)) = 0;
by(size(Linv,1)) = 0;
Ux=Linv*bx;
Uy=Linv*by;
U=[Ux(1:(size(Ux,1)-1),:),Uy(1:(size(Uy)-1),:)];
end

function E=Energy(EV,t,U,C,R)
E=0;
for i=1:size(t,1)
    for j=0:2
        j1=j+1;
        j2=mod(j+1,3)+1;
        j3=mod(j+2,3)+1;
        idx2=t(i,j2);
        idx3=t(i,j3);
        Uij=U(idx3,:)'-U(idx2,:)';
        Eij(1,1)=EV(i,j1,1);
        Eij(2,1)=EV(i,j1,2);
        rot(1,1)=R(i,1);
        rot(1,2)=R(i,2);
        rot(2,1)=R(i,3);
        rot(2,2)=R(i,4);
        E=E+C(i,j1)*norm(Uij-rot*Eij)^2;
   end
end
end
```